

Article

Synergistic Effect of Ni and Cu on the Microstructure, Corrosion Properties and Mechanical Properties of As-Cast Biomedical Co-Based Alloy

Ruoxian Wang¹ and Erlin Zhang^{1,2,*}

¹ Key Laboratory for Anisotropy and Texture of Materials, Education Ministry of China, School of Materials Science and Engineering, Northeastern University, Shenyang 110819, China

² Research Center for Metallic Wires, Northeastern University, Shenyang 110819, China

* Correspondence: zhangel@atm.neu.edu.cn; Tel./Fax: +86-24-83689400

Abstract: The microstructure, phase component, corrosion resistance, microhardness, and mechanical property of the as-cast CoCrW-(0~5)Ni-(1~4)Cu alloys were investigated to reveal the synergistic effect of Ni and Cu by using X-ray diffraction, scanning electron microscopy, electron probe microanalysis, microhardness tests, and compression tests. The alloys exhibited coarse grains consisting of dendritic substructures. No precipitate was observed in the alloys, but dendritic segregation of Cu in the interdendritic regions and grain boundaries was observed. The phase component of all alloys consists of γ phase and ϵ phase; the ϵ phase fraction decreased with increasing Ni or Cu content. The corrosion resistance of these alloys decreased with increasing Cu content when the Cu content was greater than 1 wt.%. The addition of Cu or Ni reduced the hardness significantly. The compressive yield strength showed an increasing tendency with increasing Cu content, but the influence of Ni content on compressive yield strength was limited. The results demonstrated that it should be feasible to fabricate a new biomedical CoCrWNiCu alloy by regulating Ni and Cu content, which should be a new development direction of Co-based alloy.

Keywords: CoCrWNiCu alloys; Cu element; Ni element; solidification segregation; corrosion resistance; mechanical property



Citation: Wang, R.; Zhang, E.

Synergistic Effect of Ni and Cu on the Microstructure, Corrosion Properties and Mechanical Properties of As-Cast Biomedical Co-Based Alloy. *Metals* **2022**, *12*, 1322. <https://doi.org/10.3390/met12081322>

Academic Editor: Bruno Alexandre Pacheco de Castro Henriques

Received: 24 June 2022

Accepted: 3 August 2022

Published: 6 August 2022

Publisher's Note: MDPI stays neutral with regard to jurisdictional claims in published maps and institutional affiliations.



Copyright: © 2022 by the authors. Licensee MDPI, Basel, Switzerland. This article is an open access article distributed under the terms and conditions of the Creative Commons Attribution (CC BY) license (<https://creativecommons.org/licenses/by/4.0/>).

1. Introduction

Biomedical Co-based alloys with excellent corrosion resistance, mechanical properties, and biocompatibility have been widely used as dental implants, orthopedic implants, and metallic stents [1,2]. In recent years, metallic stents used for decreasing blockages in coronary arteries have had remarkable significance in treating cardiovascular and cerebrovascular diseases [3]. Commonly, stainless steel, titanium, and Co-based alloys have been widely used to fabricate metallic stents [4]. 316L stainless steel is the most common metal used for stent applications due to its excellent mechanical properties and corrosion resistance [5]. However, 316L stainless steel is a kind of non-magnetic resonance imaging compatible material, and the poor biocompatibility of 316L stainless is an urgent problem need to deal with [4]. Ti and its alloys have high yield strength and excellent biocompatibility, but the tensile strength of Ti is significantly lower than that of Co-based alloys, which means there is a higher probability of tensile failure with Ti stents [6,7]. The mechanical properties of these alloys are listed in Table 1.

It should be noted that Co-based alloys have garnered great attention as a result of their excellent elastic modulus. Based on this aspect, Co-based alloys could be used to manufacture ultra-thin struts with high radial strength and good ductility simultaneously [8–10]. Co-based alloys are magnetic resonance imaging compatible, which is superior to other alloys such as stainless steel [11]. Furthermore, the L-605 (Co20Cr15W10Ni, wt.%) alloy used for metallic stents has been approved by the Food and Drug Administration (FDA) [4].

The requirement for the nickel element content in 316L stainless steel and the L-605 alloy is 10~14 and 9~11 (wt.%), respectively; however, the International Agency for Research on Cancer and the National Toxicology Program reported that nickel and nickel compounds are reasonably believed to be a human carcinogen [12]. Therefore, the development of a Ni-free or low Ni content alloy is extremely urgent.

Table 1. Mechanical properties of stainless steel, titanium, and Co-Cr alloys.

Alloys	Elastic Modulus/GPa	Yield Strength/MPa	Tensile Strength/MPa	Density/ $\text{g}\cdot\text{cm}^{-3}$	Ref.
Co-Cr (ASTM F90)	210	448–648	951–1220	9.2	[4,7]
316L stainless steel	190	331	586	7.9	[4,7]
Ti (ASTM F67)	110	485	760	4.5	[4,7]
Ti-6Al-4V	116	896	965		[7]
Fe-18Cr-12Mn-0.39N		1010	1150		[13]

P. Behjati et al. designed a new Ni-free austenitic stainless steel (Fe-18Cr-12Mn-0.39N) with ultrahigh strength and high ductility [13]. Jie Liu et al. proved that the effect of N on Fe-Cr-Ni alloys was more distinct compared with Ni in terms of stacking-fault energy, which was inextricably linked to the formation of austenite [14]. Furthermore, Joseph et al. investigated the possibility of the replacement of Ni with Mn, Mo, and N in austenitic stainless steels. They found that nickel was not essential for the formation of nitrogen-rich modified layers in the low temperature plasma nitriding process, which is used to increase the wear resistance of austenitic stainless steels [15]. Among all these situations, the effect of nickel in these alloy systems mainly promotes the formation of austenite. Kenta Yamanaka et al. investigated the phase stability of Co-(5~55)Ni-19Cr-9Mo (wt.%) alloys with different Ni contents [16] and found that the phase component of 15Ni~55Ni alloys was a single γ -phase. After tensile fracture, strain induced martensite could be found only in the 5Ni and 15Ni alloy. No strain induced martensite was detected in the high-Ni content samples. However, there are hardly any investigations focused on the influence of nickel content on the phase stability of the CoCrW alloy system.

There are several austenitic stabilization elements which could decrease the martensite transformation temperature and retard the martensite transformation of Co-based alloys, such as N, C, Ni, and Cu [17,18]. Among these elements, Cu has been widely used to design a new Cu-bearing metal-based antibacterial biomaterial in recent years [19]. The addition of Cu in stainless steel could not only improve the corrosion resistance [20] and tensile strength of stainless steel [21], but also conduce to reduce in-stent restenosis [22]. As is well known, in-stent restenosis is the main problem in the employment of metallic stents. Ti-Cu alloys exhibit a good mechanical property, corrosion resistance, a strong antibacterial property, and excellent cytocompatibility, in which Ti_2Cu precipitation plays a key role [19,23,24]. Furthermore, Cu could promote the formation of austenite in stainless steel and Co-based alloys [18,21], leading to the possibility that nickel could be replaced by copper in L-605 alloy. Rehman et al. investigated the influence of the addition of Cu in place of Ni on the Ti shape memory alloys [25]. They found that the mechanical properties of Cu-containing alloys were higher than that of the Cu-free alloy and the martensite start temperatures increased with increasing Cu concentration. The shape-memory properties were enhanced by the addition of Cu up to 10%. However, in order to confirm the possibility of replacing nickel with copper in L-605 alloy, the synergistic effect of Ni and Cu on the microstructure and properties of the as-cast biomedical CoCrW alloy should be investigated first.

In addition, the corrosion resistance of biomaterial is an important issue. The elemental constitute of alloy is an important influence factor on corrosion resistance; conversely, the corrosion resistance is more influenced by the property of passive film formed on the alloy surface [3]. For example, Hanawa found that Fe was preferentially released from stainless steel and Co was preferentially released from a Co-based alloy [26]. Meanwhile, biomateri-

als with strong corrosion-resistant oxide surfaces could improve their biocompatibility by reducing their metal ion release [3].

In this study, we aim to investigate the synergistic effect of Ni and Cu on the microstructure evolution, corrosion resistance, and mechanical properties of biomedical as-cast Co-based alloy. We systematically analyzed the relationship among the microstructure, phase component, corrosion resistance, and mechanical properties. The results demonstrated that it could develop a new biomedical material by controlling the Ni and Cu contents in a CoCrWNiCu alloy.

2. Materials and Methods

2.1. Alloys Preparation

Commercial pure cobalt (Co, 99.9%), chromium (Cr, 99.9%), and tungsten (W, 99.9%) were used to prepare the ingots of Co-20Cr-15W alloy and Co-23Cr-17W alloy by vacuum suspension melting furnace. Then, the Co-20Cr-15W alloy, Co-23Cr-17W alloy, pure nickel (Ni, 99.9%), and copper (Cu, 99.9%) were melted in a vacuum arc furnace to prepare the Co-Cr-W-xNi-yCu alloys ($x = 0/3/5$, $y = 0/1/2/4$, wt.%). The chemical composition of the prepared alloys is listed in Table 2. The alloys with different Ni or Cu contents were abbreviated as, for example, CoCrW, CoCrW-3Ni-1Cu, CoCrW-5Ni-4Cu, and so on.

Table 2. Chemical composition of CoCrW-xNi-yCu alloys (wt.%).

Alloys	Co	Cr	W	Ni	Cu
CoCrW	Bal.	21.0	14.6	-	-
CoCrW-1Cu	Bal.	20.7	14.1	-	0.9
CoCrW-2Cu	Bal.	20.4	14.0	-	1.9
CoCrW-4Cu	Bal.	21.6	14.7	-	3.9
CoCrW-3Ni-1Cu	Bal.	21.6	14.4	3.2	1.0
CoCrW-3Ni-2Cu	Bal.	20.0	14.0	3.2	1.9
CoCrW-3Ni-4Cu	Bal.	20.5	14.7	3.3	3.8
CoCrW-5Ni-1Cu	Bal.	20.7	14.5	5.3	1.0
CoCrW-5Ni-2Cu	Bal.	19.3	14.0	5.1	1.9
CoCrW-5Ni-4Cu	Bal.	21.7	14.3	5.2	3.8

2.2. Microstructure Observation

A disk specimen ($\Phi 15 \text{ mm} \times 2 \text{ mm}$) for microstructure observation was cut from the ingots by wire cutting and ground with SiC emery papers up to 3000 grits. The phase component of alloys was analyzed on D/MAX-RB X-ray diffractometer (Rigaku, Tokyo, Japan) with a measurement range of 2θ as 40° to 100° . The JCPDS (The Joint Committee on Powder Diffraction Standards) card numbers used to identify XRD (X-ray diffraction) phases in this paper were PDF#15-0806 for γ phase and PDF#05-0727 for ϵ phase (PDF: Powder Diffraction File). The relative fraction of the considered phase was estimated by the formula [27]:

$$f^{\text{PhaseA}}(\%) = \frac{\sum I_{\text{peaksA}}}{\sum I_{\text{peaksTot}}} \times 100 \quad (1)$$

where A is the considered phase, the numerator is the sum of the intensities of all the peaks belonging to the considered phase, and the denominator is the sum of the intensities of all peaks. For example, to calculate the relative fraction of the ϵ phase, the numerator in this equation was the sum of integrated intensities of all peaks of the ϵ phase, while the denominator was the sum of the integrated intensities of all peaks in both phases.

Microstructure observation and composition analysis were performed by JSM7800F field-emission scanning electron microscopy (SEM, Japan Electron Optics Laboratory, Tokyo, Japan) and JXA8530F field-emission electron probe microanalysis (EPMA, Japan Electron Optics Laboratory, Tokyo, Japan). Samples were electrolytic etched in $\text{H}_2\text{O}_2:\text{HCl} = 6:1$ aqueous solution for 30 s at a voltage of 6 V, while the samples for EPMA were electrolytic etched for 5 s.

2.3. Electrochemical Test

The electrolyte solution used for the corrosion resistance test was 0.9% NaCl solution. A water bath heater was used to maintain the temperature of the electrolyte solution at 37 ± 1 °C. A three-electrode system was used to evaluate the electrochemical properties. The electrochemical impedance spectroscopy (EIS) test was conducted after an open circuit potential (OCP) test, which lasted for 1 h. Then, the Tafel curves were obtained at a scan rate of 1 mV/s.

2.4. Mechanical Properties

The Vickers hardness meter (MH-500, Wuxi Deep Instrument Equipment Co., Ltd., Wuxi, China) was used to test the micro-hardness of alloys. The test load was 500 g and the duration time was 10 s. Ten different fields were selected randomly. Samples for a compression test were prepared with a dimension of $8 \times 8 \times 10$ mm³. The measurement was carried out on AG-Xplus electronic universal testing machine (Shimadzu, Tokyo, Japan) with a speed of 1 mm/min.

3. Results

3.1. Microstructure

SEM images of the CoCrW-yCu alloys (Figure 1a–d), CoCrW-3Ni-yCu alloys (Figure 1e–g), and CoCrW-5Ni-yCu alloys (Figure 1h–j) are shown in Figure 1. Typical dendrites formed in all alloys, regardless of the Ni or Cu content. The variation of dendritic thicknesses was mainly caused by the different sampling position on different ingots. The ingots investigated in this study were fabricated in a vacuum arc furnace. The microstructure of the conventional cast alloy was usually inhomogeneous. The samples were cut from ingots randomly, which might cause different dendritic thicknesses. Meanwhile, the melting point and diffusion coefficient of different elements and the solidification rate would affect the dendritic thicknesses. The grain boundary of CoCrW-xNi-4Cu ($x = 0/3/5$) alloys was more obvious compared with other alloys. Many etching pits, which were mainly distributed in the interdendritic space, could be seen in CoCrW-xNi-4Cu ($x = 0/3/5$) alloys. However, no precipitate was found in any samples. This result shows that no significant change was observed in the microstructure among alloys with different Ni contents, while the grain boundary was more obvious in the alloys with high Cu content.

Figures 2 and 3 show the SEM images and element composition maps for the CoCrW-4Cu alloy at low-magnification and high-magnification, respectively. They revealed distinct solidification segregation, where Cu and Cr were enriched in the interdendritic regions. Figure 3 shows a trigeminal grain boundary, which shows that the partial grain boundary was a Cu-depleted region, but the appearance of Cu depletion was not found in the white elliptical region; however, our previous studies found that Cu was slightly enriched near the grain boundary in the Co₂₀Cr₁₅W₁₀Ni-Cu alloy and Co₂₇Cr₆Mo-Cu alloy, while Co and Ni were completely miscible [28,29]. Therefore, it can be deduced that Cu was mainly segregated at the grain boundary. During the electrolytic etching process, partial Cu that is enriched at grain boundaries might dissolve, which leads to the Cu-depleted region at grain boundary. There was no sign of precipitates, which is in accordance with SEM results. The influence of Cu content on the microstructure was mainly embodied in the region of the grain boundary and etching pits, which might be caused by dendritic segregation. The grain boundary was more easily etched by CoCrW-xNi-4Cu ($x = 0/3/5$) alloys compared with other alloys.

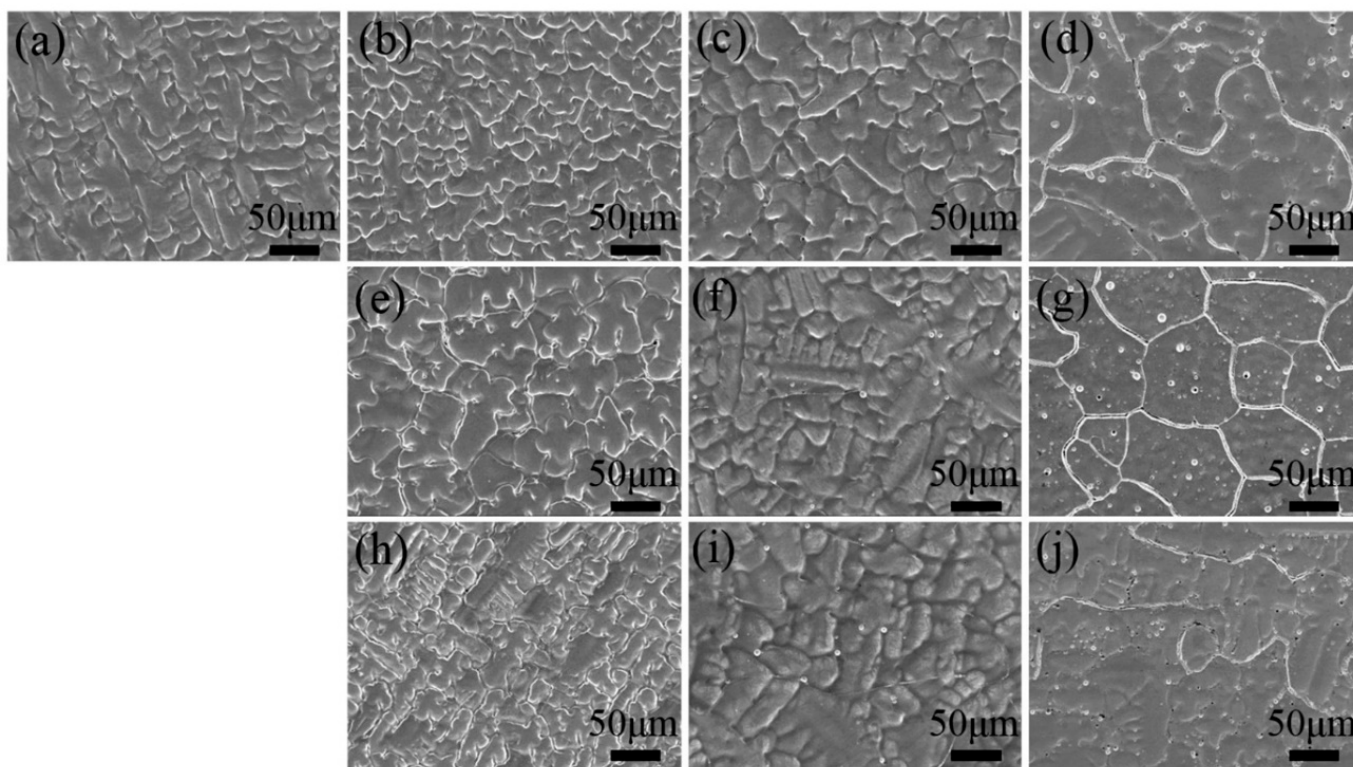


Figure 1. SEM images of the as-cast CoCrW-xNi-yCu alloys: (a) CoCrW, (b) CoCrW-1Cu, (c) CoCrW-2Cu, (d) CoCrW-4Cu, (e) CoCrW-3Ni-1Cu, (f) CoCrW-3Ni-2Cu, (g) CoCrW-3Ni-4Cu, (h) CoCrW-5Ni-1Cu, (i) CoCrW-5Ni-2Cu, and (j) CoCrW-5Ni-4Cu alloys.

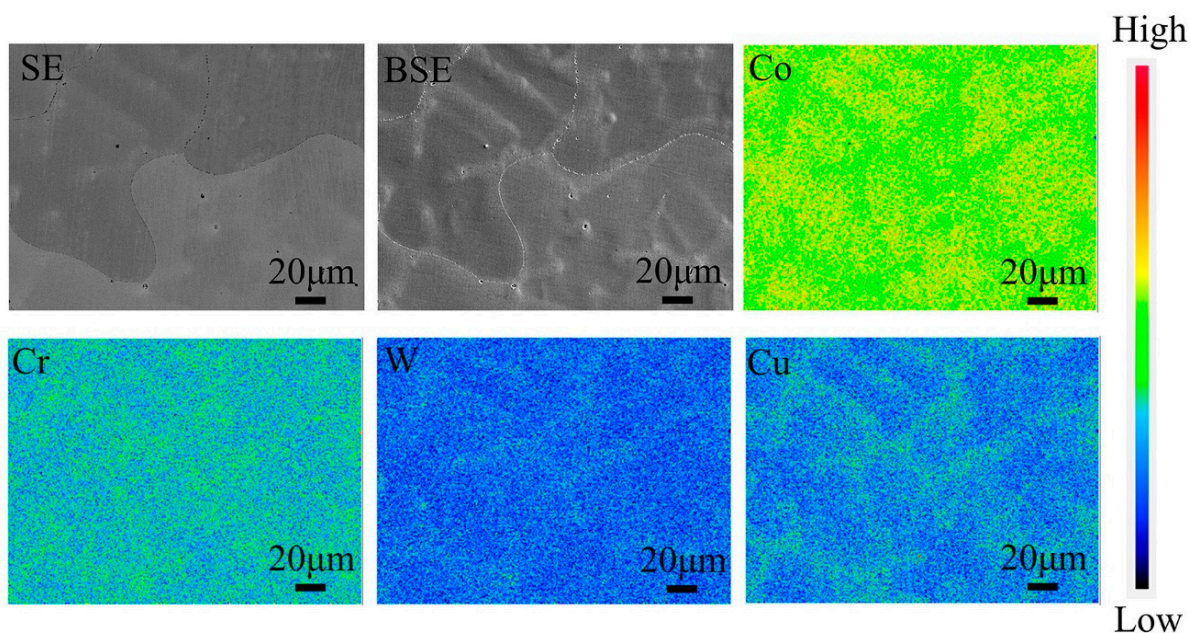


Figure 2. SEM images and corresponding EPMA elemental maps of the CoCrW-4Cu alloy at low magnification. (SE: Secondary electron; BSE: Backscattered electron).

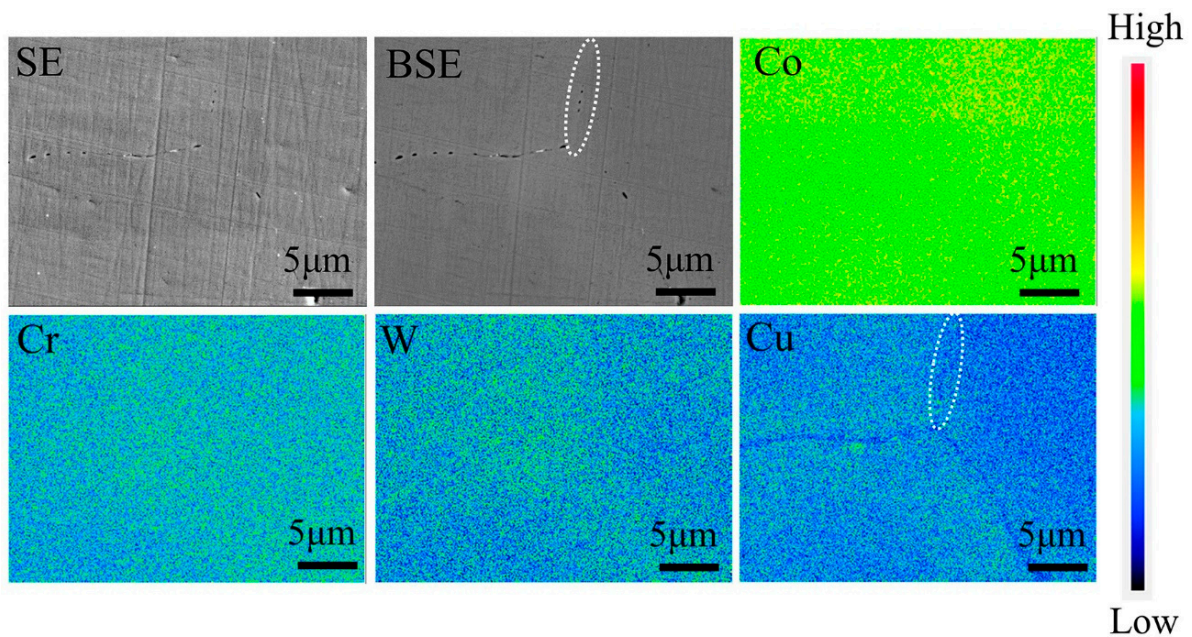


Figure 3. SEM images and corresponding EPMA elemental maps of the CoCrW-4Cu alloy at high magnification. (The white circle marked grain boundary).

3.2. Phase Identification

Figure 4 shows XRD profiles of the as-cast CoCrW- x Ni- y Cu alloys. XRD patterns show that both γ phase and ϵ phase were found in all samples. Strong peaks originating from the γ phase were observed in most alloys such as CoCrW-1Cu, CoCrW-4Cu, CoCrW-3Ni-1Cu, and CoCrW-5Ni-1Cu alloys, which means that the fraction of the γ phase in these alloys was relatively high. Table 3 lists the calculated volume fraction (%) of the ϵ phase in different alloys. In the CoCrW- y Cu alloy, the calculated volume fraction of the ϵ phase decreased from 24.9% to 17.0% by increasing Cu content. The situation of CoCrW-3/5Ni- y Cu alloys was consistent with the CoCrW- y Cu alloy, which indicates that increasing the Cu content could reduce the fraction of the ϵ phase and increase the fraction of the γ phase. Furthermore, adding Ni could also decrease the fraction of the ϵ phase. For instance, the calculated volume fraction of ϵ phase decreased from 18.5% to 15.7% by increasing Ni content in the CoCrW- x Ni-1Cu alloy ($x = 0/3/5$); thus, the enhancement of Ni or Cu content could retard the martensite transformation and decrease the fraction of the ϵ phase and increase the fraction of the γ phase.

Table 3. The calculated volume fraction (%) of hcp ϵ -phase in the as-cast CoCrW- x Ni- y Cu alloys.

Alloys	0Cu	1Cu	2Cu	4Cu
0Ni	24.9	18.5	17.3	17.0
3Ni	-	17.4	16.6	15.7
5Ni	-	15.7	15.6	14.5

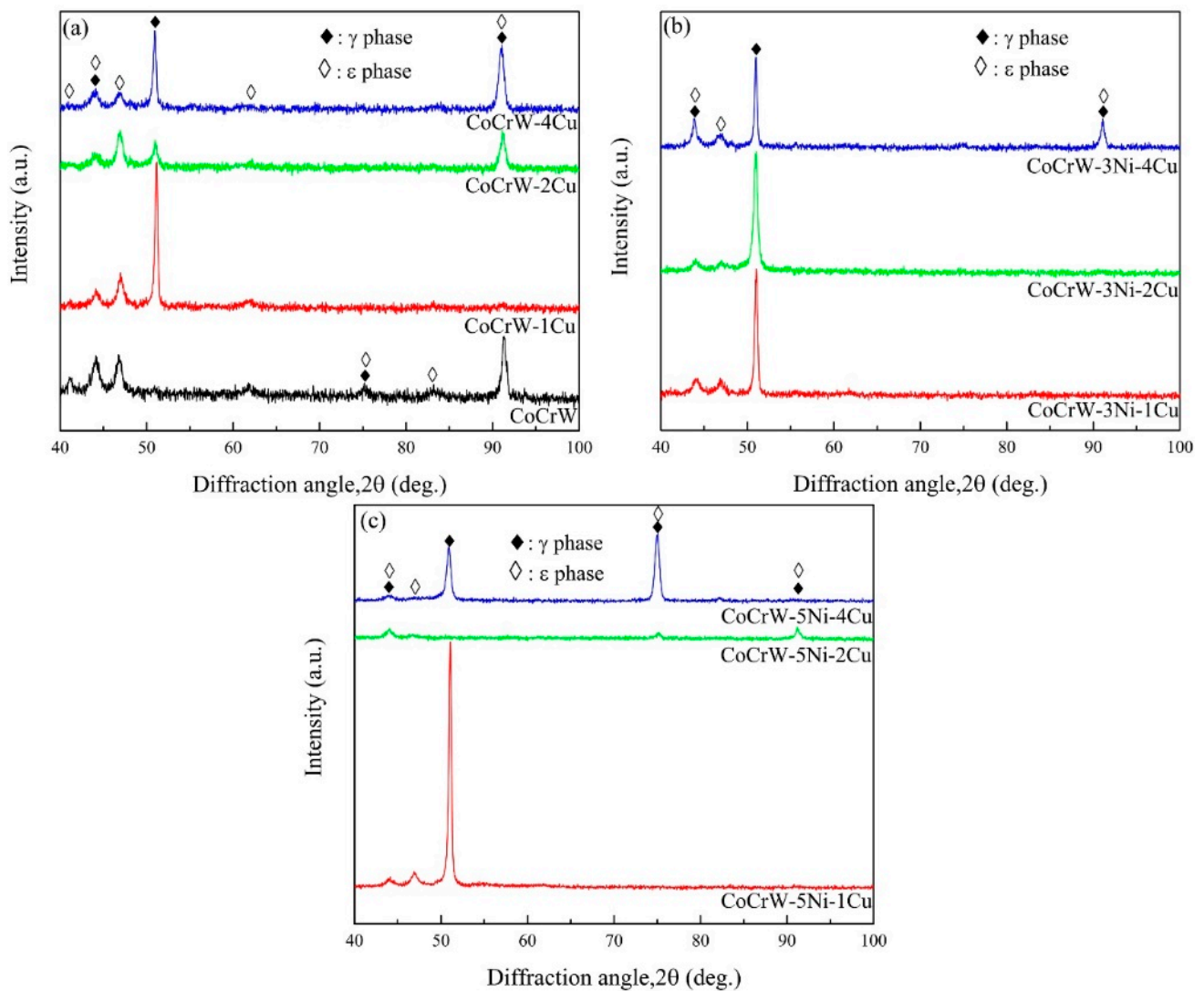


Figure 4. XRD patterns of the as-cast CoCrW-xNi-yCu alloys.

3.3. Electrochemical Test

Figure 5a,c,e shows the OCP vs immersion time of CoCrW-xNi-yCu alloys in a 0.9% NaCl solution. The OCP value rapidly increased and reached a near steady state at the initial stage of immersion, which originated from the formation and growth of a passive film. Figure 5b,d,f shows the polarization curves of CoCrW-xNi-yCu alloys. The polarization curves displayed similar trends for all alloys. There was a small but distinct active-passive transition in CoCrW-xNi-4Cu ($x = 0/3/5$) alloys, which indicates that these alloys could not spontaneously be passivated. As the potential increased, active-passive transition occurred due to the formation of the protective Cr substance [30]. When the potentials became more positive, the corrosion rate increased and reached the maximum, at which time more insoluble corrosion products formed and caused a sudden drop in the corrosion current density. The rate of anodic reaction was controlled by the dynamic formation and dissolution of such corrosion products [31]. The active-passive transition might be caused by the repetitive partial dissolution and reprecipitation of the surface oxide film on the materials in an aqueous solution [26]. Table 4 lists the electrochemical parameters obtained from the OCP and Tafel curves. When the Ni content was constant but the Cu content increased, the E_{OCP} and E_{corr} moved towards a positive direction. The i_{corr} of the CoCrW-xNi-yCu alloys increased with increasing Cu content when the Cu content was greater than 1 wt.%. For example, the i_{corr} value of the CoCrW-3Ni-1Cu alloy was lower

than that of the CoCrW-3Ni-2/4Cu alloys. However, the i_{corr} of the CoCrW alloy was the highest among these alloys.

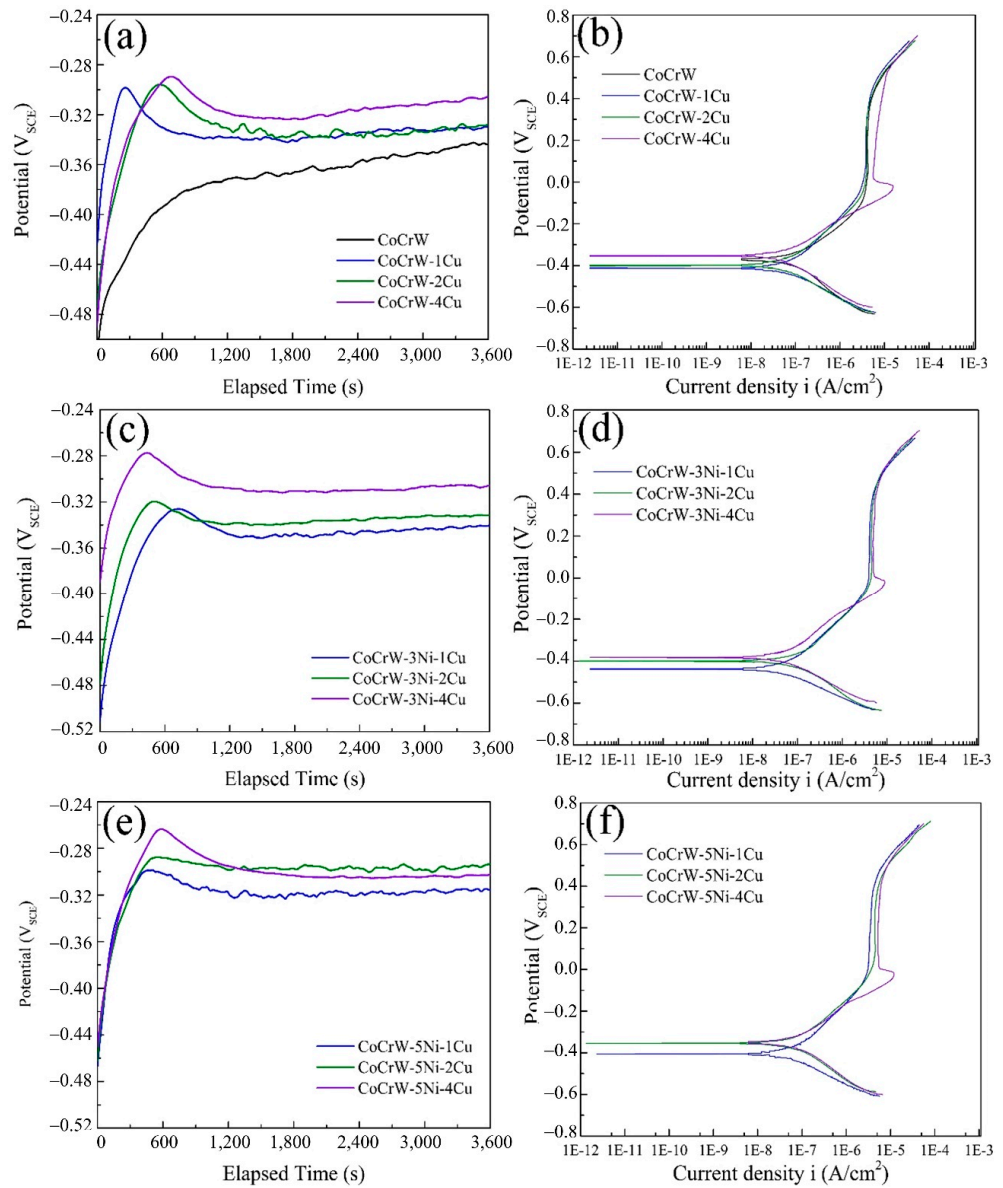


Figure 5. (a,c,e) Open-circuit potential (OCP) and (b,d,f) Tafel curves of the as-cast CoCrW-xNi-yCu alloys: (a,b) CoCrW-yCu, (c,d) CoCrW-3Ni-yCu, and (e,f) CoCrW-5Ni-yCu alloys.

Table 4. Electrochemical data obtained from OCP curves and polarization curves.

Alloys	E_{OCP} (mV)	E_{corr} (mV)	i_{corr} (nA/cm ²)
CoCrW	-343.82 ± 4.01	-372.22 ± 18.74	73.42 ± 9.45
CoCrW-1Cu	-337.38 ± 9.41	-411.60 ± 14.36	47.14 ± 6.75
CoCrW-2Cu	-328.18 ± 2.38	-398.72 ± 11.86	53.46 ± 4.54
CoCrW-4Cu	-305.48 ± 16.03	-353.32 ± 27.58	71.51 ± 10.93
CoCrW-3Ni-1Cu	-340.44 ± 9.15	-437.67 ± 23.46	46.70 ± 1.97
CoCrW-3Ni-2Cu	-331.24 ± 10.51	-400.87 ± 28.58	60.27 ± 10.31
CoCrW-3Ni-4Cu	-306.09 ± 9.25	-382.15 ± 35.69	63.15 ± 8.59
CoCrW-5Ni-1Cu	-315.91 ± 15.74	-405.16 ± 24.02	52.05 ± 10.77
CoCrW-5Ni-2Cu	-293.52 ± 32.09	-353.94 ± 49.69	60.33 ± 3.83
CoCrW-5Ni-4Cu	-302.72 ± 20.65	-351.48 ± 30.31	60.61 ± 5.93

Figure 6a,c,e shows the Nyquist diagrams of the as-cast CoCrW-xNi-yCu alloys. All samples exhibited a characteristic single capacitive. The circular arc radius was reduced by increasing Cu content when the Cu content was greater than 1 wt.%. Furthermore, the CoCrW alloy showed a smaller circular arc than the Cu-containing CoCrW alloys.

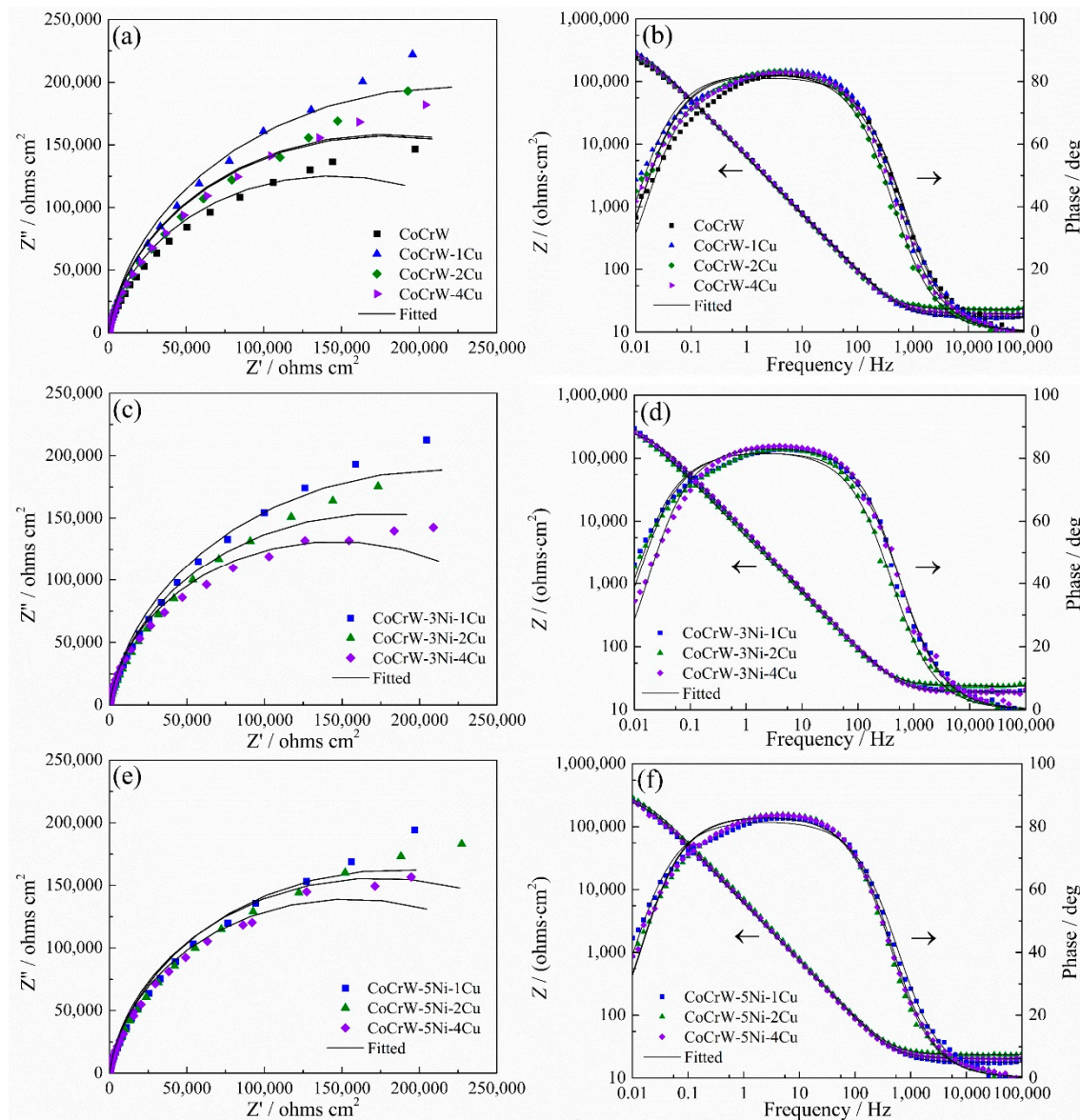


Figure 6. (a,c,e) Nyquist plot diagram, (b,d,f) Bode and Bode phase plot diagram of the as-cast CoCrW-xNi-yCu alloys: (a,b) CoCrW-yCu, (c,d) CoCrW-3Ni-yCu and, (e,f) CoCrW-5Ni-yCu alloys.

Figure 6b,d,f shows the variation of the Bode and Bode phase plot diagram of the as-cast CoCrW-xNi-yCu alloys. There were some indications that a typical capacitive behavior occurred in the surface of samples. For instance, the value of Z was almost constant in the high frequency region, whereas the phase angle was near zero degree. The slope of the absolute impedance curve was close to -1 in association with a phase angle near 80° in the middle and low frequency regions. Therefore, ZSimpWin software was used to fit the EIS data and an $R_s(QR_p)$ equivalent circuit was selected.

Table 5 summarizes the electrochemical data obtained from EIS curves. The solution resistance (R_s) values were close to $20 \Omega \cdot \text{cm}^2$ for all samples in normal saline. The value of R_p was reduced by increasing Cu content when the Cu content was greater than 1 wt.%. On the contrary, the variation of the R_p was very small when the Ni content changed. The

R_p of the The CoCrW alloy was the lowest among CoCrW-yCu alloys; therefore, it can be concluded that the influence of Cu content was more severe than the influence of Ni content on the corrosion resistance. However, the corrosion resistance of the CoCrW-1Cu alloy was higher than that of the CoCrW alloy, which means that proper Cu could enhance corrosion resistance while excess Cu would reduce corrosion resistance. The change in Ni content did not visibly affect the corrosion resistance.

Table 5. Electrochemical data obtained from EIS curves after fitting using ZsimpWin software.

Alloys	R_s ($\Omega \cdot \text{cm}^2$)	CPE ($\mu\text{F} \cdot \text{cm}^{-2}$)	n	R_p ($\text{k}\Omega \cdot \text{cm}^2$)
CoCrW	18.89 ± 1.01	39.76 ± 3.42	0.9114 ± 0.0048	274.43 ± 17.91
CoCrW-1Cu	19.68 ± 1.88	33.01 ± 2.85	0.9126 ± 0.0110	440.37 ± 50.63
CoCrW-2Cu	20.07 ± 2.56	37.73 ± 0.95	0.9159 ± 0.0052	352.73 ± 17.74
CoCrW-4Cu	19.61 ± 0.28	36.53 ± 0.31	0.9151 ± 0.0027	292.43 ± 46.73
CoCrW-3Ni-1Cu	21.35 ± 2.09	38.69 ± 1.75	0.9160 ± 0.0030	431.87 ± 5.11
CoCrW-3Ni-2Cu	22.28 ± 1.77	39.20 ± 3.49	0.9162 ± 0.0022	349.23 ± 38.76
CoCrW-3Ni-4Cu	20.39 ± 1.15	35.86 ± 4.35	0.9263 ± 0.0053	339.73 ± 66.52
CoCrW-5Ni-1Cu	19.44 ± 1.30	36.34 ± 2.62	0.9146 ± 0.0057	422.60 ± 42.41
CoCrW-5Ni-2Cu	23.69 ± 0.13	34.86 ± 2.35	0.9254 ± 0.0041	358.80 ± 10.78
CoCrW-5Ni-4Cu	20.33 ± 0.62	35.53 ± 3.43	0.9243 ± 0.0047	347.90 ± 38.56

3.4. Mechanical Properties

Figure 7 shows the change in microhardness of the as-cast CoCrW-xNi-yCu alloys. The addition of Cu reduced the hardness significantly but no difference was found among the alloys with different Cu contents. Meanwhile, the addition of Ni also reduced the hardness in a content dependent way. The compressive stress-strain curves and compressive yield strength are shown in Figure 8. It can be concluded that all samples showed good ductility; only CoCrW-xNi-4Cu ($x = 0/3/5$) alloys were fractured at the final stage of the test. The yield strength of the CoCrW alloy was relatively higher compared with the CoCrW-1Cu alloy. For Cu-containing alloys, the yield strength showed an increasing tendency when increasing the Cu content; however, the influence of Ni content on yield strength was limited and the influence of Cu content on mechanical properties was more severe than that of the Ni content.

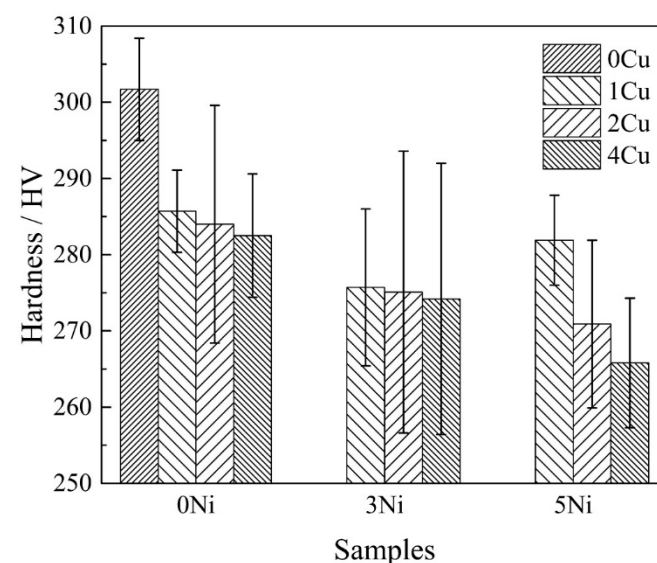


Figure 7. Microhardness of the as-cast CoCrW-xNi-yCu alloys.

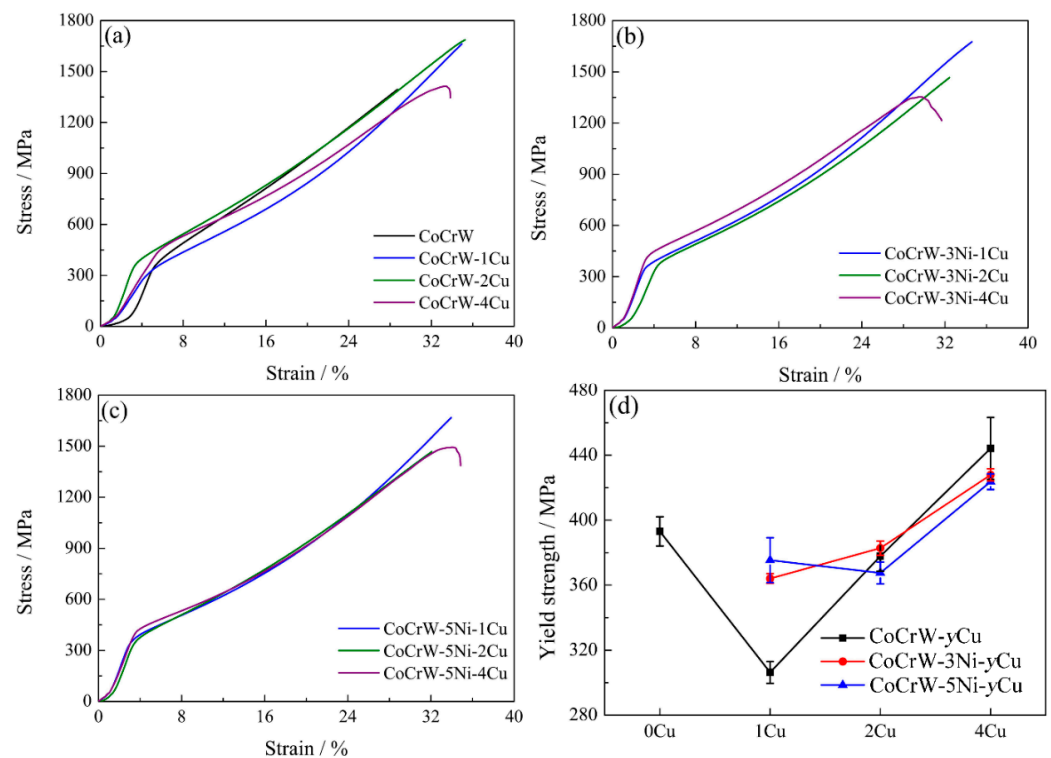


Figure 8. (a–c) Typical compressive stress-strain curves and (d) Compressive yield strength of as-cast CoCrW-xNi-yCu alloys.

4. Discussion

In general, martensite transformation (fcc phase to hcp phase) is often induced during the solidification process for as-cast Co-based alloys, which means the γ phase is stable at high temperatures while the ϵ phase is stable at room temperature [26,32,33]. XRD analysis revealed that γ phase and ϵ phase were simultaneously confirmed in the as-cast CoCrW-xNi-yCu alloys. No diffraction peak of other precipitate phase was found. Strong peaks belong to the γ -phase were observed in the CoCrW-1Cu, CoCrW-4Cu, CoCrW-3Ni-1/2/4Cu, and CoCrW-5Ni-1Cu alloys. It has been proven that the addition of nickel or copper could stabilize the γ phase of Co-based alloys [18,28,29]. Although some diffraction peaks of γ phase and ϵ phase were very close, such as the peaks around 44° , 75° , and 92° , it can be recognized that the phase constitution of these alloys was mainly γ -phase even in the CoCrW alloy, which was confirmed by the calculated results of the volume fraction (%) of hcp ϵ phase of the as-cast CoCrW-xNi-yCu alloys. Therefore, Cu and Ni could retard the martensite transformation of the as-cast Co-based alloy. Yang et al. investigated the stacking fault energy of different binary Co-based alloys with a computational thermodynamic approach and first principles density functional theory calculations [34,35]. They found that alloying with Fe, Ni, and Mn atoms could increase the stacking fault energy while alloying with Mo and Cr atoms could decrease the stacking fault energy. The formation of the stacking fault is regarded as the beginning of martensite transformation in Co-based alloys [36]. Chiba et al. found that the presence of nano precipitates (Cr_2N) and the short-range order of Cr and N atoms could suppress the athermal martensitic transformation in the γ -phase of the CoCrMoN alloy [37]. Zhang et al. also found a Cu-rich phase that could retard the martensitic transformation in the CoCrMoCu alloy [18]. However, a single γ -phase structure has not been found even in the CoCrWNiCu alloy with highest Ni and Cu content in this paper. It should be noted that the phase constitution of the CoCrW-10Ni alloy and CoCrW-10Ni-4Cu alloy was mainly composed of γ phase and a little ϵ phase [29]. Therefore, the variation of Ni or Cu content in the as-cast CoCrW-xNi-yCu alloys did not have a strong impact on the phase constitution because the fraction of the hcp ϵ phase of the as-cast CoCrW alloy was relatively small.

The SEM results in Figure 1 indicate that all alloys exhibited a coarse dendritic structure without any precipitates. It should be noted that the grain boundary of CoCrW-xNi-4Cu ($x = 0/3/5$) alloys emerged after electrolytic etching while other alloys did not. In order to explore the solidification segregation, the EPMA analysis of the CoCrW-4Cu alloy was conducted. The EPMA results in Figures 2 and 3 revealed that the interdendritic region and grain boundary were enriched with Cu. Generally, as-cast alloys mainly exhibit a characteristic dendritic structure caused by solidification conditions and alloy chemical composition. Tungsten is a type of refractory metal, while the melting point of copper is just 1083 °C. In this situation, dendritic segregation is easily formed. It can be concluded from the Co-Cu and Cr-Cu binary phase diagram that Cu is nearly undissolved in Co or Cr at room temperature [28]; however, there is no intermetallic compound that could form between Cu and Co/Cr, but Ni could be totally dissolved in Co [18]. Therefore, the segregation of the Cu element can be formed more easily in this alloy system. Kenta Yamanaka et al. investigated the solidification segregation of N-containing Co-33Cr-9W alloys [1] and found that the interdendritic regions were enriched with Cr and W, but depleted of Co. Zhang et al. also found dendritic segregation of Cu element in the as-cast CoCrMoCu alloys and CoCrWNiCu alloys [28,29]. They also found that Cu was enriched slightly at the grain boundaries, which is in line with the results of Figure 3.

In addition to solidification segregation, many intermetallic compounds could be found in the as-cast Co-based alloys like σ -phase and R-phase [1,32]. Several studies focused on improving the strength and ductility of as-cast Co-based alloys by adding nitrogen and carbon and so on [32,38]. In these studies, chromium-rich intermetallic compound and R-phase were found in addition to solidification segregation. However, there was no any sign of the intermetallic compound in the as-cast CoCrW-xNi-yCu alloys. In summary, the change of Ni content has no significant influence on microstructure. Meanwhile, the segregation of Cu and its migration into the interdendritic regions during solidification did not cause any precipitation of the intermetallic compound.

It is interesting that copper depletion at the grain boundary was found in Figure 3, which was caused by the dissolution of Cu during electrolytic etching process. As is well known, chromium depleted regions at the grain boundary in many stainless steels are commonly reported [39,40]. T. Thorvaldsson et al. found chromium-depleted zones formed at the grain boundaries of niobium and titanium stabilized austenitic stainless steels after ageing treatment [41]. Generally, the formation of chromium depleted regions is often associated with the precipitation of chromium-rich phases [39,41,42]; however, no Cu-enriched precipitate was found in the as-cast CoCrW-xNi-yCu alloys. Therefore, copper depleted zones caused by a Cu-enriched precipitate was not likely to be formed in this alloy system.

The corrosion resistance of alloys is closely related to their microstructure. The corrosion resistance of CoCrW-xNi-yCu alloys was reduced by increasing Cu content when the Cu content was greater than 1 wt.%. Furthermore, the corrosion resistance of the CoCrW alloy is the lowest among these alloys, which means that proper Cu addition could enhance corrosion resistance; however, the variation of corrosion resistance caused by different Ni content of alloys was limited.

The influence of different chemical compositions on the corrosion resistance of CoCrW-xNi-yCu alloys is closely related to the Ni content and Cu content, respectively. Conversely, Ni content could not visibly affect the corrosion resistance. J.H. Potgieter et al. found that increasing the nickel content of duplex stainless steel could increase its pitting resistance in sodium chloride [43], which originated from the presence of the passive nickel oxide layer. However, Munoz et al. noted that this passive nickel oxide layer did not comparatively enhance the passivation properties in halide environments because the film could be destroyed by replacing the oxygen position with halide ions in the film [43,44]. Furthermore, S. Azuma et al. found that the resistance of 4% Ni ferritic steel was higher than that of 0% Ni ferritic steel and 30% Ni austenitic steel in the seawater immersion test, which was mainly due to its higher pitting potential and lower depassivation pH [45]. In this paper,

although the Ni content varied from 0 wt.% to 5 wt.%, the solidification segregation of Ni element was not apparent. Therefore, the corrosion resistance did not change distinctly with increasing or reducing Ni content.

Conversely, the corrosion resistance of the CoCrW-1Cu alloy is higher than that of the CoCrW alloy. Nevertheless, increasing Cu content could decrease the corrosion resistance if the Ni content was 0 wt.%, 3 wt.%, or 5 wt.%. These results should be mainly attributed to the dendritic segregation of Cu. Figures 2 and 3 showed that Cu was enriched in the interdendritic region and grain boundary, which means that there were lots of Cu-rich regions in these alloy systems. As is well known, the presence of a chromium depleted region could decrease the corrosion resistance of the metallic alloys [46–50]. Similarly, the Cu-rich regions might be responsible for the decreased corrosion resistance of the alloys in this paper. The standard potential of the Cu/Cu²⁺ couples is obviously nobler than other elements in these alloy systems, which is the reason why the corrosion resistance of the CoCrW-1Cu alloy is higher than that of the CoCrW alloy. The standard potential of the Ni/Ni²⁺ and Co/Co²⁺ couples was very close. Therefore, galvanic corrosion was generated between the Cu-rich region and matrix in the electrochemical testing. The galvanic corrosion was more severe when the Cu content increased, which was deleterious for corrosion resistance. The Cu-rich region might break the uniform passive oxide (Cr₂O₃) [29,51–53]; thus, the corrosion resistance of CoCrW-xNi-yCu alloys was driven by the variation of Cu content rather than Ni content, which shows that the corrosion resistance decreased by increasing Cu content when the Cu content was greater than 1 wt.%. However, it should be noted that the corrosion resistance of all alloys was relatively close apart from CoCrW and CoCrW-0/3/5Ni-4Cu alloys.

The microhardness results showed a similar changing tendency by changing Cu or Ni content. For instance, the microhardness decreased by increasing the Cu content when Ni content remained unchanged. Similarly, the microhardness decreased by increasing the Ni content. In Co-based alloys, the hardness is related to the fraction of constituent phases and precipitates. Wei et al. found that the increase in the hcp ϵ phase proportion could increase the hardness of Co-based alloys due to the higher hardness of the ϵ phase than that of γ phase [2,54]; there was no precipitate in these alloys. However, it should be noted that the change in the microhardness was not obvious among all alloys as a result of the small change in microstructure and phase component.

In the as-cast Cu-containing Co-based alloys, the factors that might affect mechanical properties mainly consist of phase component, precipitates, solidification segregation, and the solid solubility of Cu in matrix. Firstly, the fraction of the fcc γ phase was relatively high among all alloys, which could enhance the plasticity of Co-base alloys. The ϵ phase fraction slightly decreased when increasing the Ni or Cu content in this paper. For the CoCrW-1Cu alloy, the yield strength was lower than that of the CoCrW alloy, which might be due to the fact that the ϵ phase fraction of the CoCrW-1Cu alloy was a little lower and Cu has low strength and good ductility. Li et al. found that the average grain size of the Co-(5–25)Ni-Cr-Mo alloy was approximately the same, while the ϵ phase fraction decreased by increasing the Ni content; the yield strength also decreased by increasing the Ni content [16]. However, the yield strength of Cu-containing alloys increased by increasing the Cu content, which might be related to the solidification segregation. Normally, the solid solubility of Cu in Co at room temperature was very low, while approximately 20 wt.% Cu could dissolve in Co at 1367 °C [28]. Therefore, Cu could gradually segregate during the solidification process due to its low solid solubility in matrix and low melting point. It was proven that Cu was enriched in the interdendritic regions in Figure 2. However, no precipitate was found in any alloys. Liu et al. found that the Cu precipitates with high misfit and many crystal defects in metastable austenite could improve its strength by precipitation hardening [55]. We speculate that the Cu segregation region in a Co-based alloy might have large misfit with the matrix, which could increase its alloy strength as precipitation hardening, much like the effect of Cu precipitates in the high-strength low-alloy steel. Similarly, large amounts of

Cu-rich regions might cause stress concentration during a compression test and finally lead to fracture at the end of the test.

For biomaterial, cell toxicity is a subject worthy of special attention. Zhang et al. proved that the CoCrW-10Ni-4Cu alloy exhibited as good biocompatibility as an L-605 alloy. However, the corrosion resistance of the CoCrW-10Ni-4Cu alloy was significantly lower than that of the L-605 alloy [29]. The corrosion resistance of all alloys in this paper was higher than the results of the CoCrW-10Ni-4Cu alloy; therefore, although there was no any cytocompatibility experiment in this paper, it could be reasonably inferred to that no alloy in this paper would cause cell toxicity.

In conclusion, dendritic segregation was obviously observed in the as-cast CoCrW-xNi-yCu alloys. The dendritic segregation was more severe when increasing Cu content. The ϵ phase fraction decreased by increasing the Ni or Cu content. Adding a slight amount of Cu (1wt.%) in the CoCrW alloy could enhance its corrosion resistance. Although the corrosion resistance decreased with increasing Cu content in Cu-containing alloys, it was still higher than that of the Cu-free alloy. The addition of Cu or Ni reduced the hardness significantly. The compressive yield strength showed an increasing tendency with increased Cu content for Cu-containing alloys, while the influence of Ni content on compressive yield strength was limited. The synergistic effect of Cu and Ni on the microstructure, corrosion resistance, and mechanical properties were systematically investigated. The harm of Ni as a carcinogen and the effect of Cu on reducing the occurrence of in-stent restenosis should be considered simultaneously in the design of a CoCrW-Ni-Cu alloy. However, the solidification segregation has a strong impact on the properties of Cu-containing Co-based alloys. Therefore, more investigations focused on these alloys after heat treatments are needed in the future.

5. Conclusions

- (1) The addition of Cu or Ni retarded the martensite transformation and decreased the ϵ phase fraction of the CoCrW-Ni-Cu alloy. The addition of Cu promoted the segregation of Cu at the interdendritic regions and grain boundaries.
- (2) The addition of ≤ 1 wt.% Cu would enhance the corrosion resistance of CoCrW-xNi-yCu alloys, but more Cu content would reduce it. The change in Ni content did not affect the corrosion resistance visibly.
- (3) The addition of Cu or Ni decreased the microhardness. The influence of Ni content on yield strength was limited, but the compressive yield strength showed an increasing tendency when increasing the Cu content.

Author Contributions: Conceptualization, E.Z.; Formal analysis, R.W.; Funding acquisition, E.Z.; Investigation, R.W.; Methodology, R.W.; Resources, E.Z.; Software, R.W.; Supervision, E.Z.; Validation, R.W.; Visualization, R.W.; Writing-original draft, R.W.; Writing-review & editing, E.Z. All authors have read and agreed to the published version of the manuscript.

Funding: This research was funded by National Natural Science Foundation of China, grant number 31470930 and 31971253.

Institutional Review Board Statement: Not applicable.

Informed Consent Statement: Not applicable.

Data Availability Statement: Not applicable.

Conflicts of Interest: The authors declare no conflict of interest.

References

1. Yamanaka, K.; Mori, M.; Torita, Y.; Chiba, A. Effect of nitrogen on the microstructure and mechanical properties of Co-33Cr-9W alloys prepared by dental casting. *J. Mech. Behav. Biomed. Mater.* **2018**, *77*, 693–700. [[CrossRef](#)] [[PubMed](#)]
2. Wei, D.; Koizumi, Y.; Chiba, A.; Ueki, K.; Ueda, K.; Narushima, T.; Tsutsumi, Y.; Hanawa, T. Heterogeneous microstructures and corrosion resistance of biomedical Co-Cr-Mo alloy fabricated by electron beam melting (EBM). *Addit. Manuf.* **2018**, *24*, 103–114. [[CrossRef](#)]

3. O'Brien, B.; Carroll, W. The evolution of cardiovascular stent materials and surfaces in response to clinical drivers: A review. *Acta Biomater.* **2009**, *5*, 945–958. [[CrossRef](#)] [[PubMed](#)]
4. Mani, G.; Feldman, M.D.; Patel, D.; Agrawal, C.M. Coronary stents: A materials perspective. *Biomaterials* **2007**, *28*, 1689–1710. [[CrossRef](#)] [[PubMed](#)]
5. Taylor, A. *Endoluminal Stenting*; W.B. Saunders Company: London, UK, 1996; pp. 28–33.
6. Park, J.B.; Kim, Y.K. *Biomaterials Principles and Applications*; CRC Press: Boca Raton, FL, USA, 2003; pp. 1–20.
7. Brunski, J.B. *Biomaterials Science an Introduction to Materials in Medicine*; Elsevier Academic Press: San Diego, CA, USA, 2004; pp. 137–153.
8. Briguori, C.; Sarais, C.; Pagnotta, P.; Liistro, F.; Montorfano, M.; Chieffo, A.; Sgura, F.; Corvaja, N.; Albiero, R.; Stankovic, G.; et al. In-stent restenosis in small coronary arteries: Impact of strut thickness. *J. Am. Coll. Cardiol.* **2002**, *40*, 403–409. [[CrossRef](#)]
9. Rittersma, S.Z.; de Winter, R.J.; Koch, K.T.; Bax, M.; Schotborgh, C.E.; Mulder, K.J.; Tijssen, J.G.; Piek, J.J. Impact of strut thickness on late luminal loss after coronary artery stent placement. *Am. J. Cardiol.* **2004**, *93*, 477–480. [[CrossRef](#)]
10. Kereiakes, D.J.; Cox, D.A.; Hermiller, J.B.; Midei, M.G.; Bachinsky, W.B.; Nukta, E.D.; Leon, M.B.; Fink, S.; Marin, L.; Lansky, A.J.; et al. Usefulness of a cobalt chromium coronary stent alloy. *Am. J. Cardiol.* **2003**, *92*, 463–466. [[CrossRef](#)]
11. Klocke, A.; Kemper, J.; Schulze, D.; Adam, G.; Kahl-Nieke, B. Magnetic Field Interactions of Orthodontic Wires during Magnetic Resonance Imaging (MRI) at 1.5 Tesla. *J. Orofac. Orthop.* **2005**, *66*, 279–287. [[CrossRef](#)]
12. Prueitt, R.L.; Li, W.; Chang, Y.-C.; Boffetta, P.; Goodman, J.E. Systematic review of the potential respiratory carcinogenicity of metallic nickel in humans. *Crit. Rev. Toxicol.* **2020**, *50*, 605–639. [[CrossRef](#)]
13. Behjati, P.; Kermanpur, A.; Najafzadeh, A.; Baghbadorani, H.S.; Karjalainen, P.; Jung, J.-G.; Lee, Y.-K. Design of a new Ni-free austenitic stainless steel with unique ultrahigh strength-high ductility synergy. *Mater. Des.* **2014**, *63*, 500–507. [[CrossRef](#)]
14. Liu, J.; Han, P.; Dong, M.; Fan, G.; Qiao, G.; Yang, J. Influence of Ni and N on generalized stacking-fault energies in Fe–Cr–Ni alloy: A first principle study. *Phys. B Condens. Matter* **2012**, *407*, 891–895. [[CrossRef](#)]
15. Buhagiar, J.; Li, X.; Dong, H. Formation and microstructural characterisation of S-phase layers in Ni-free austenitic stainless steels by low-temperature plasma surface alloying. *Surf. Coat. Technol.* **2009**, *204*, 330–335. [[CrossRef](#)]
16. Li, J.; Yamanaka, K.; Chiba, A. Influence of interatomic interactions on the mechanical properties of face-centered cubic multicomponent Co–Ni–Cr–Mo alloys. *Materialia* **2020**, *12*, 100742. [[CrossRef](#)]
17. Niinomi, M.; Narushima, T.; Nakai, M. *Advances in Metallic Biomaterials*; Springer: Berlin, Germany, 2015; pp. 157–159.
18. Wang, R.; Qin, G.; Zhang, E. Effect of Cu on Martensite Transformation of CoCrMo alloy for biomedical application. *J. Mater. Sci. Technol.* **2020**, *52*, 127–135. [[CrossRef](#)]
19. Zhang, E.L.; Fu, S.; Wang, R.X.; Li, H.X.; Liu, Y.; Ma, Z.Q.; Liu, G.K.; Zhu, C.S.; Qin, G.W.; Chen, D.F. Role of Cu element in biomedical metal alloy design. *Rare Met.* **2019**, *38*, 476–494. [[CrossRef](#)]
20. Liu, H.; Xu, D.; Yang, K.; Liu, H.; Cheng, Y.F. Corrosion of antibacterial Cu-bearing 316L stainless steels in the presence of sulfate reducing bacteria. *Corros. Sci.* **2018**, *132*, 46–55. [[CrossRef](#)]
21. Ye, D.; Li, J.; Jiang, W.; Su, J.; Zhao, K. Effect of Cu addition on microstructure and mechanical properties of 15%Cr super martensitic stainless steel. *Mater. Des.* **2012**, *41*, 16–22. [[CrossRef](#)]
22. Ren, L.; Xu, L.; Feng, J.; Zhang, Y.; Yang, K. In vitro study of role of trace amount of Cu release from Cu-bearing stainless steel targeting for reduction of in-stent restenosis. *J. Mater. Sci. Mater. Electron.* **2012**, *23*, 1235–1245. [[CrossRef](#)]
23. Cao, S.; Zhang, Z.-M.; Zhang, J.-Q.; Wang, R.-X.; Wang, X.-Y.; Yang, L.; Chen, D.-F.; Qin, G.-W.; Zhang, E.-L. Improvement in antibacterial ability and cell cytotoxicity of Ti–Cu alloy by anodic oxidation. *Rare Met.* **2021**, *41*, 594–609. [[CrossRef](#)]
24. Zhang, E.; Zhao, X.; Hu, J.; Wang, R.; Fu, S.; Qin, G. Antibacterial metals and alloys for potential biomedical implants. *Bioact. Mater.* **2021**, *6*, 2569–2612. [[CrossRef](#)]
25. Rehman, S.U.; Khan, M.; Khan, A.N.; Ali, L.; Jaffery, S.I.H.; Khurram, M. Quaternary alloying of copper with Ti50Ni25Pd25 high temperature shape memory alloys. *Mater. Sci. Eng. A* **2019**, *763*. [[CrossRef](#)]
26. Hanawa, T. Metal ion release from metal implants. *Mater. Sci. Eng. C* **2004**, *24*, 745–752. [[CrossRef](#)]
27. Balagna, C.; Spriano, S.; Faga, M.G. Characterization of Co–Cr–Mo alloys after a thermal treatment for high wear resistance. *Mater. Sci. Eng. C* **2012**, *32*, 1868–1877. [[CrossRef](#)] [[PubMed](#)]
28. Zhang, E.; Liu, C. A new antibacterial Co–Cr–Mo–Cu alloy: Preparation, biocorrosion, mechanical and antibacterial property. *Mater. Sci. Eng. C* **2016**, *69*, 134–143. [[CrossRef](#)] [[PubMed](#)]
29. Wang, R.; Wang, R.; Chen, D.; Qin, G.; Zhang, E. Novel CoCrWNi alloys with Cu addition: Microstructure, mechanical properties, corrosion properties and biocompatibility. *J. Alloys Compd.* **2020**, *824*, 153924. [[CrossRef](#)]
30. Wang, Z.; Feng, Z.; Fan, X.-H.; Zhang, L. Pseudo-passivation mechanism of CoCrFeNiMo0.01 high-entropy alloy in H₂S-containing acid solutions. *Corros. Sci.* **2020**, *179*, 109146. [[CrossRef](#)]
31. Zhu, W.; Zhao, C.; Zhou, J.; Kwok, C.T.; Ren, F. Microstructure, sliding wear and corrosion behavior of bulk nanostructured Co–Ag immiscible alloys. *J. Alloys Compd.* **2018**, *748*, 961–969. [[CrossRef](#)]
32. Yamanaka, K.; Mori, M.; Chiba, A. Effects of carbon concentration on microstructure and mechanical properties of as-cast nickel-free Co–28Cr–9W-based dental alloys. *Mater. Sci. Eng. C* **2014**, *40*, 127–134. [[CrossRef](#)]
33. Lu, Y.; Wu, S.; Gan, Y.; Li, J.; Zhao, C.; Zhuo, D.; Lin, J. Investigation on the microstructure, mechanical property and corrosion behavior of the selective laser melted CoCrW alloy for dental application. *Mater. Sci. Eng. C* **2015**, *49*, 517–525. [[CrossRef](#)]

34. Achmad, T.L.; Fu, W.; Chen, H.; Zhang, C.; Yang, Z.-G. Effects of alloying elements concentrations and temperatures on the stacking fault energies of Co-based alloys by computational thermodynamic approach and first-principles calculations. *J. Alloys Compd.* **2017**, *694*, 1265–1279. [[CrossRef](#)]
35. Achmad, T.L.; Fu, W.; Chen, H.; Zhang, C.; Yang, Z.G. First-principles calculations of generalized-stacking-fault-energy of Co-based alloys. *Comput. Mater. Sci.* **2016**, *121*, 86–96. [[CrossRef](#)]
36. Wang, C.; Wang, H.; Huang, T.; Xue, X.; Qiu, F.; Jiang, Q. Generalized-stacking-fault energy and twin-boundary energy of hexagonal close-packed Au: A first-principles calculation. *Sci. Rep.* **2015**, *5*, 10213. [[CrossRef](#)] [[PubMed](#)]
37. Yamanaka, K.; Mori, M.; Chiba, A. Nanoarchitected Co–Cr–Mo orthopedic implant alloys: Nitrogen-enhanced nanostructural evolution and its effect on phase stability. *Acta Biomater.* **2013**, *9*, 6259–6267. [[CrossRef](#)] [[PubMed](#)]
38. Yamanaka, K.; Mori, M.; Chiba, A. Developing high strength and ductility in biomedical Co–Cr cast alloys by simultaneous doping with nitrogen and carbon. *Acta Biomater.* **2016**, *31*, 435–447. [[CrossRef](#)]
39. Lee, K.M.; Cho, H.S.; Choi, D.C. Effect of isothermal treatment of SAF 2205 duplex stainless steel on migration of δ/γ interface boundary and growth of austenite. *J. Alloys Compd.* **1999**, *285*, 156–161. [[CrossRef](#)]
40. Kaneko, K.; Fukunaga, T.; Yamada, K.; Nakada, N.; Kikuchi, M.; Saghi, Z.; Barnard, J.S.; Midgley, P.A. Formation of M23C6-type precipitates and chromium-depleted zones in austenite stainless steel. *Scr. Mater.* **2011**, *65*, 509–512. [[CrossRef](#)]
41. Thorvaldsson, T.; Dunlop, G.L. Grain boundary Cr-depleted zones in Ti and Nb stabilized austenitic stainless steels. *J. Mater. Sci.* **1983**, *18*, 793–803. [[CrossRef](#)]
42. Weiss, B.; Stickler, R. Phase instabilities during high temperature exposure of 316 austenitic stainless steel. *Met. Mater. Trans. A* **1972**, *3*, 851–866. [[CrossRef](#)]
43. Potgieter, J.; Olubambi, P.; Cornish, L.; Machio, C.; Sherif, E.-S.M. Influence of nickel additions on the corrosion behaviour of low nitrogen 22% Cr series duplex stainless steels. *Corros. Sci.* **2008**, *50*, 2572–2579. [[CrossRef](#)]
44. Muñoz, A.I.; Antón, J.G.; Guiñón, J.L.; Herranz, V.P. Effects of solution temperature on localized corrosion of high nickel content stainless steels and nickel in chromated LiBr solution. *Corros. Sci.* **2006**, *48*, 3349–3374. [[CrossRef](#)]
45. Azuma, S.; Kudo, T.; Miyuki, H.; Yamashita, M.; Uchida, H. Effect of nickel alloying on crevice corrosion resistance of stainless steels. *Corros. Sci.* **2004**, *46*, 2265–2280. [[CrossRef](#)]
46. Matula, M.; Hyspecka, L.; Svoboda, M.; Vodarek, V.; Dagbert, C.; Galland, J.; Stonawska, Z.; Tuma, L. Intergranular corrosion of AISI 316L steel. *Mater. Charact.* **2001**, *46*, 203–210. [[CrossRef](#)]
47. Bouchet, D.; Priester, L. Indirect detection of grain-boundary segregation of carbon in iron-chromium alloys (Cr 10%) by electrochemical study. *J. Mater. Sci.* **1979**, *14*, 2205–2214. [[CrossRef](#)]
48. Moura, V.; Lima, L.; Pardal, J.M.; Kina, A.; Corte, R.; Tavares, S. Influence of microstructure on the corrosion resistance of the duplex stainless steel UNS S31803. *Mater. Charact.* **2008**, *59*, 1127–1132. [[CrossRef](#)]
49. Mulford, R.A.; Hall, E.L.; Briant, C.L. Sensitization of Austenitic Stainless Steels II. Commercial Purity Alloys. *Corrosion* **1983**, *39*, 132–143. [[CrossRef](#)]
50. Was, G.S.; Tischner, H.H.; Latanision, R.M. The influence of thermal treatment on the chemistry and structure of grain boundaries in Inconel 600. *Metall. Trans. A* **1981**, *12*, 1397–1408. [[CrossRef](#)]
51. Hanawa, T.; Hiromoto, S.; Asami, K. Characterization of the surface oxide film of a Co–Cr–Mo alloy after being located in quasi-biological environments using XPS. *Appl. Surf. Sci.* **2001**, *183*, 68–75. [[CrossRef](#)]
52. Matković, T.; Matković, P.; Malina, J. Effects of Ni and Mo on the microstructure and some other properties of Co–Cr dental alloys. *J. Alloys Compd.* **2004**, *366*, 293–297. [[CrossRef](#)]
53. Qian, C.; Wu, X.; Zhang, F.; Yu, W. Electrochemical impedance investigation of Ni-free Co–Cr–Mo and Co–Cr–Mo–Ni dental casting alloy for partial removable dental prosthesis frameworks. *J. Prosthet. Dent.* **2016**, *116*, 112–118. [[CrossRef](#)]
54. García, A.D.J.S.; Medrano, A.M.; Rodríguez, A.S. Formation of hcp martensite during the isothermal aging of an fcc Co–27Cr–5Mo–0.05C orthopedic implant alloy. *Met. Mater. Trans. A* **1999**, *30*, 1177–1184. [[CrossRef](#)]
55. Liu, S.; Rong, X.; Guo, H.; Misra, R.; Jin, X.; Shang, C. Reinforced Cu precipitation strengthening by matrix transformation from martensite to austenite in high-strength low-alloy steel. *Mater. Sci. Eng. A* **2021**, *825*, 141783. [[CrossRef](#)]